*buildings*

MDPI

*Article*

# Study on Restoring Force Model of Plate-Reinforced Composite Coupling Beam with Small Span-to-Depth Ratio

**Yan Ma [1,*], Licheng Ma [1], Hua Lu [1], Xiaotong Ma [1], Yuting Qu [2], Yong Zhao [2] and Jianbo Tian [2]**

[1] School of Civil Engineering, North Minzu University, Yinchuan 750021, China; 2024507@nmu.edu.cn (L.M.); 2013101@nmu.edu.cn (H.L.); 2015039@nun.edu.cn (X.M.)
[2] School of Civil Engineering and Architecture, Xi'an University of Technology, Xi'an 710048, China; 18833292014@163.com (Y.Q.); zhaoyong211015@163.com (Y.Z.); tianjianbo@xaut.edu.cn (J.T.)
* Correspondence: my13895313525@163.com

**Abstract**

Coupling beams are critical connecting components in coupled shear wall systems and core tube structures. At the same time, they play an important role when the structure is subjected to an earthquake. Plate-reinforced composite (PRC) coupling beams exhibit superior comprehensive performance in terms of bearing capacity, deformation performance, energy dissipation capacity, and construction efficiency. However, research on PRC coupling beams remains limited both domestically and internationally. To better describe the structural response of steel plate–concrete composite coupling beams, this study collected existing experimental data. The beams had a small span-to-depth ratio. The loading was cyclic. The study normalized the skeleton curves of each specimen. The span-to-depth ratio ranged from 0.9 to 2.5. The plate ratio ranged from 3% to 5%. For these beams, preliminary skeleton curve fitting equations are proposed. The equations are based on existing data. The equations apply to two types of composite coupling beams. One type uses a steel plate and ordinary concrete. The other type uses a steel plate and fiber concrete. These equations are derived using a trilinear model and linear fitting tools. Furthermore, restoring force models for steel plate–conventional concrete and steel plate–fiber concrete composite coupling beams with a small span-to-depth ratio are proposed. Comparative analysis shows that each model captures the hysteretic response of PRC coupling beams with acceptable accuracy in the elastic and decline phases, while the elastic–plastic stage is suitable only for trend prediction. It should be noted that the proposed models are preliminary engineering approximations primarily applicable within the following ranges: a span-to-depth ratio of 0.9~2.5, a plate ratio of 3~5%, concrete strength of C30~C50, a longitudinal reinforcement ratio of 0.86~2.23%, a stirrup ratio of 0.56~0.63%, and a steel plate thickness of 6~10 mm. For configurations significantly outside these ranges, additional experimental validation is required.

**Keywords:** plate-reinforced composite coupling beam; skeleton curve; seismic performance; hysteresis rule

Check for updates

Academic Editor: Eric M. Lui

Received: 3 April 2026
Revised: 16 May 2026
Accepted: 19 May 2026
Published: 25 May 2026

**Copyright:** © 2026 by the authors. Licensee MDPI, Basel, Switzerland. This article is an open access article distributed under the terms and conditions of the Creative Commons Attribution (CC BY) license.

## 1. Introduction

Earthquakes are unpredictable and possess immense destructive power, posing significant threats to human habitats and societal development. Therefore, it is extremely important to improve the seismic performance of building structures. In high-rise buildings, coupling beams serve as crucial connecting elements in shear wall systems, frame–shear

wall structures, and core tube configurations, acting as the primary defense against seismic forces [1]. However, due to their relatively small span-to-height ratios, these beams are prone to brittle shear failures. Thus, the energy dissipation capacity of the whole building is reduced, and the seismic performance is reduced.

Researchers have extensively studied methods to enhance the seismic performance of coupling beams in high-rise structures. Lam and Su [2,3] introduced shear studs on both sides of steel plates to improve the interaction between concrete and steel plates. Their findings indicate that these shear studs effectively prevented bond-slip between the steel plates and concrete, thereby enhancing the seismic performance of composite coupling beams. Hou et al. [4] conducted quasi-static tests to assess the effects of parameters such as span-to-depth ratio, steel plate reinforcement ratio, and plate configuration on coupling beams. The results demonstrate that embedded steel plates significantly improved the seismic performance of these beams. Similarly, Tian et al. [5] performed quasi-static tests considering the influence of span-to-depth ratio on coupling beams. The study concluded that the installation of embedded steel plates effectively enhanced the bearing capacity of coupling beams.

In recent years, advancements in concrete materials have led to the widespread adoption and development of fiber-reinforced concrete (FRC) [6]. To enhance the ductility of coupling beams, numerous researchers both domestically and internationally have investigated the seismic performance of these beams using FRC. Scholars such as Shin [7], Canbolat [8], Zhao et al. [9], Hu et al. [10], and Liang et al. [11] have studied the span-to-depth ratio of coupling beams with varying reinforcement and matrix materials. Their findings indicate that FRC effectively inhibits the appearance and development of cracks during loading, while also improving the beams' bearing capacity, energy dissipation capacity, and ductility performance. Additionally, Hou et al. [12] and Deng et al. [13] conducted quasi-static tests on composite coupling beams made of steel plates and super toughness concrete. Their results demonstrate that both high-toughness concrete and FRC exhibit strong synergistic performance with embedded steel plates, significantly enhancing the seismic performance of composite coupling beams. In a study of seismic performance of coupling beams, Jafari et al. [14] systematically analyzed the effects of axial compression ratio, initial prestressing ratio, and span-to-depth ratio. They focused on cyclic response, stiffness degradation, and damage evolution. Their work revealed differences in failure modes and ultimate states between deep and shallow coupling beams. In addition, the structural reliability of joints directly affects the mechanical behavior of coupling beams. Szymczak-Graczyk et al. [15] presented engineering cases. They pointed out that overly dense reinforcement or inadequate concrete compaction in joint regions can significantly reduce the load capacity of members. This finding provides a warning for the design and construction of end joints of coupling beams.

The restoring force model is a mathematical framework used to describe the seismic performance of structures under cyclic loading. Che et al. [16] designed FRC diagonal stirrup coupling beam specimens with varying aspect ratios, conducted low-cycle repeated loading tests, observed failure modes, and proposed a trilinear restoring force model. Comparisons with experimental results showed that the trilinear model's calculated curve closely matched the test skeleton curve. Li et al. [17] simulated the hysteretic curves of diagonal stirrup engineered cementitious composite (ECC) coupling beam specimens and proposed a shear hinge restoring force model for such beams. Mou et al. [18] and Song et al. [19] established restoring force models for steel beam to CFST/HSS column joints with a reinforced concrete slab and for connections in innovative hybrid coupled wall systems, respectively. These models were developed by considering strength and stiffness degradation laws and employing regression analysis. In nonlinear analysis and simplified modeling of reinforced concrete members, methods based on homogenization theory can effectively

balance computational efficiency and accuracy. Staszak et al. [20] proposed a numerical homogenization method for three-layer slab structures. They combined this method with an analytically derived shear correction factor. Their simplified model achieved good consistency with three-dimensional models in predicting global deformation. Garbowski et al. [21] further conducted scale model tests of bubble deck slabs and three-dimensional finite element modeling. They verified the reliability of two homogenization techniques. These techniques are numerical homogenization and cross-sectional spatial integration. Both techniques can predict the overall deflection of members reliably. This work provides a methodological reference for a simplified analysis of restoring force models of complex structures.

Generally, the restoring force model consists of two components: the skeleton curve and the hysteretic rule. The skeleton curve describes the seismic performance of the structure at key points on the load–displacement curve, while the hysteretic rule characterizes the structure's behavior under cyclic loading.

To date, restoring force models for this type of composite coupling beam are scarce; most studies focus only on experimental phenomena or load capacity. As a preliminary attempt to describe the cyclic response of steel plate–concrete composite coupling beams with a small span-to-depth ratio, this study establishes two separate restoring force models based on existing data [22–25]: one for steel plate–conventional concrete beams, and another for steel plate–fiber-reinforced concrete beams. Both adopt a trilinear skeleton curve.

## 2. Experimental Program

### *2.1. Test Specimens*

In the design of 11 coupling beam specimens [22–25], various factors were considered to evaluate their impact on seismic performance. These factors included section size, span-to-depth ratio, longitudinal reinforcement ratio, stirrup ratio, steel plate reinforcement ratio, steel plate sectional height, steel plate section thickness, and matrix material. The specimens comprised 8 steel plate–conventional concrete composite coupling beams and 3 steel plate–fiber-reinforced concrete composite coupling beams with a small span-to-depth ratio. The specific values for each parameter are detailed in Table 1.

**Table 1.** The value of each parameter of the specimens.

| Number of Specimens | Section Size | Span-to-Depth Ratio | Longitudinal Reinforcement Ratio (%) | Stirrup Ratio (%) | Steel Plate Reinforcement Ratio (%) | Height of Steel Plate $h_w$ (mm) | Plate Thickness $t_w$ (mm) | Matrix Material |
|---|---|---|---|---|---|---|---|---|
| PRC-NS1 | 160 × 320 | 1.5 | 1.67 | 0.63 | 4.61 | 260 | 8 | Conventional concrete |
| PRC-CB1 | 180 × 350 | 1.5 | 1.65 | 0.56 | 3.07 | 290 | 6 | Conventional concrete |
| PRC-CB2 | 180 × 350 | 1.5 | 1.65 | 0.56 | 4.09 | 290 | 8 | Conventional concrete |
| PRC-CB3 | 180 × 350 | 1.5 | 1.65 | 0.56 | 5.11 | 290 | 10 | Conventional concrete |
| PRC-CB6 | 180 × 350 | 0.9 | 1.65 | 0.56 | 4.09 | 290 | 8 | Conventional concrete |
| PRC-CB7 | 180 × 350 | 2.0 | 1.65 | 0.56 | 4.09 | 290 | 8 | Conventional concrete |
| CB-1.5 [22] | 120 × 400 | 1.5 | 1.12 | 0.56 | 4.21 | 320 | 6 | Conventional concrete |
| CB-2.5 [22] | 120 × 400 | 2.5 | 2.23 | 0.56 | 4.21 | 320 | 6 | Fiber-reinforced concrete |
| PRCB-2 | 160 × 320 | 1.5 | 0.86 | 0.63 | 4.42 | 260 | 8 | Fiber-reinforced concrete |
| DB-1.5 [22] | 120 × 400 | 1.5 | 1.12 | 0.56 | 4.21 | 320 | 6 | Fiber-reinforced concrete |
| DB-2.5 [22] | 120 × 400 | 2.5 | 2.23 | 0.56 | 4.21 | 320 | 6 | Fiber-reinforced concrete |

To accurately simulate the coupling effect between the actual wall panel and the steel plate–concrete composite coupling beams with a small span-to-depth ratio, each coupling beam specimen was equipped with an embedded steel plate coupling wall panel. To enhance the bonding between the steel plate and concrete, anchoring studs were installed on the embedded steel plates in both the coupling beam and the wall limb. This design significantly improved the synergistic interaction between the embedded steel plate and the fiber-reinforced concrete while reducing the bond-slip effect. Additionally, the steel plate embedded in the coupling beam was welded to ensure effective anchorage within the wall limb concrete. The geometric dimensions and reinforcement details of the coupling beam specimens from references [22–25] are illustrated in the accompanying Figure 1.

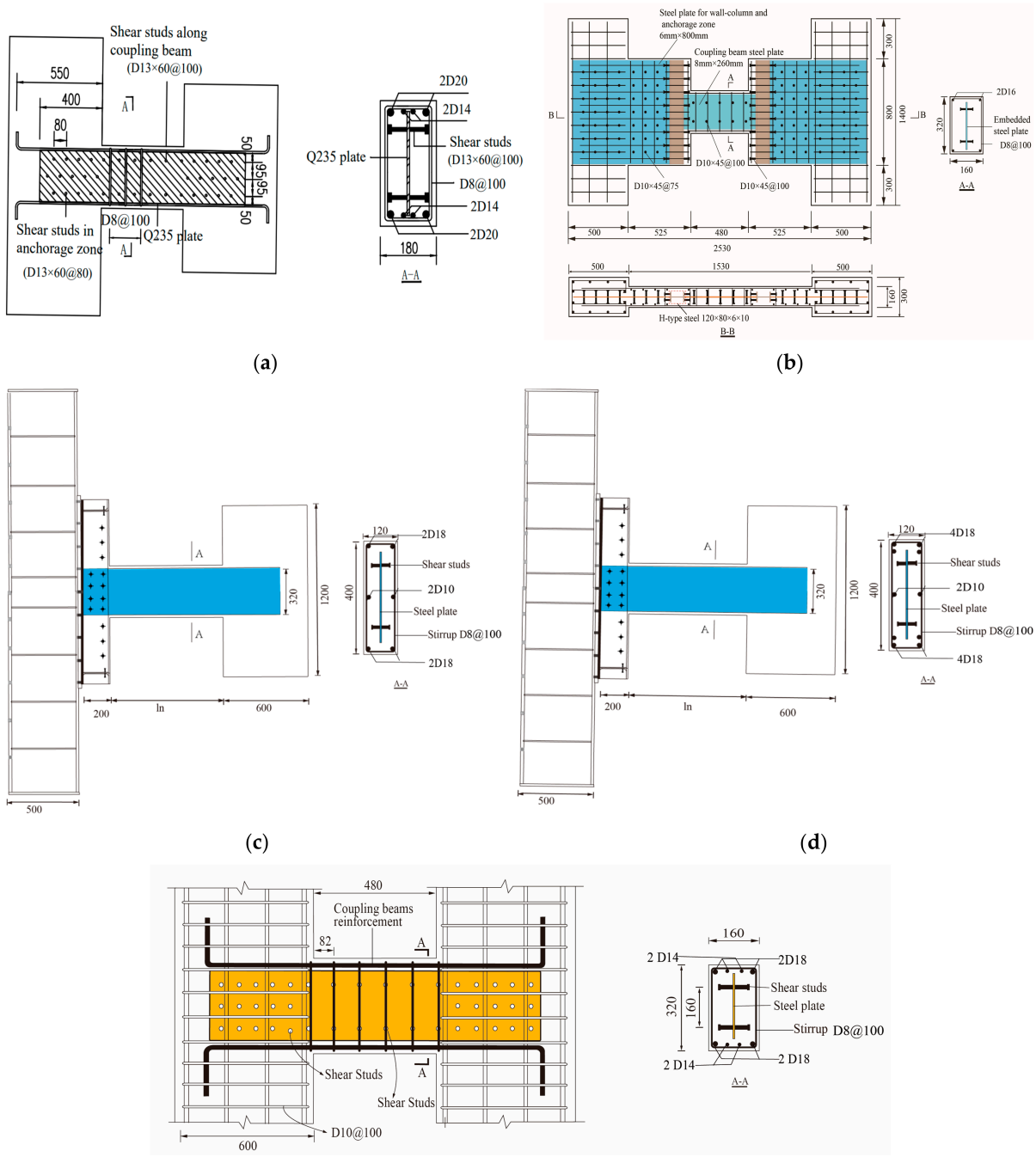
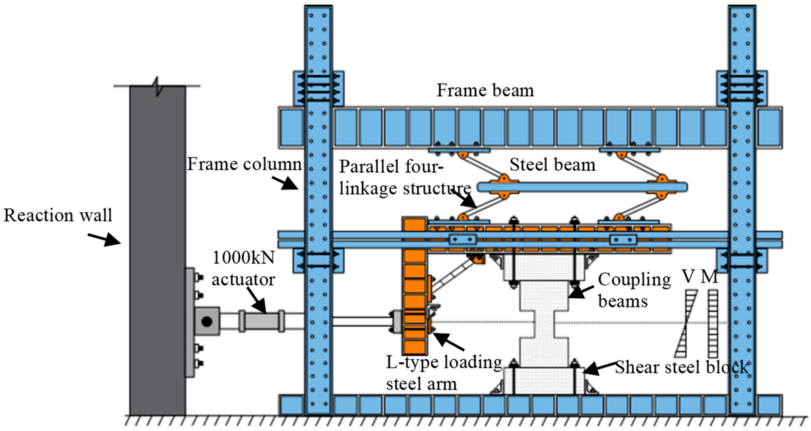



**Figure 1.** Specimen size. (**a**) PRC-CB1~PRC-CB3 and PRC-CB6~PRC-CB7. (**b**) PRCB-2. (**c**) CB-1.5 and DB-1.5 [22]. (**d**) CB-2.5 and DB-2.5 [22]. (**e**) PRC-NS1.

### 2.2. Test Loading Protocol

In this test, a construction research-type loading equipment was used, and a 1000 kN horizontal actuator applied low-cyclic loading to the coupling beam specimen. The loading protocol in this study follows the requirements of the 'Specification for Seismic Test Methods of Buildings' (JGJ101-96) [26]. Horizontal loading was applied using a hybrid load–displacement control method. Before yielding the specimen, load control was used. Each loading step was 30 kN, with one cycle per step. Yielding was considered to have occurred when the load–displacement curve showed a clear turning point. After yielding, displacement control was adopted. The same displacement was repeated for three cycles. The displacement increment was 3 mm. The test was terminated when the load capacity of the specimen dropped below 85% of the ultimate load. At this point, the specimen was judged to have failed.

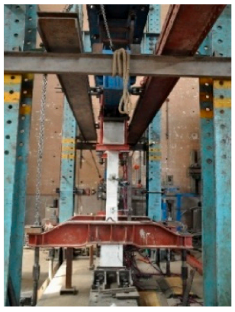
To induce shearing functions, the actuator's horizontal action ray passed through the middle span of the specimen. Shear keys were installed on both sides of the up and down end blocks to maximize the stability of the connection between the specimen and the loading equipment. Additionally, a parallel four-linkage device and an out-of-plane constraint wheel were positioned on the top of the coupling beam and on both its front and back sides. These components ensured planar movement along the load direction while preventing out-of-plane instability, thereby maintaining the precision of the shear test. Figure 2 presents the schematic and actual loading device.




(**a**) Diagrammatic drawing



(**b**) Test setup (South)



(**c**) Test setup (East)

**Figure 2.** Laboratory loading device and schematic diagram.

### 2.3. Measurement Content

In this test, a load–displacement mixed control system was employed. Load control was used during the elasticity phase of the specimen. Displacement control was applied after yielding. During the experiment, several types of data were measured. These included

the horizontal load imposed by the actuator. Displacements at both ends of the beam were also measured using hysteresis displacement meters.

To measure the relative linear displacement ($\Delta$) at both ends, the transducers were installed at the midpoint of the upper block and fixed to the steel frame of the lower block, which was securely connected to the lower block. This setup ensured that the influence of bottom sliding on the test results could be neglected. To measure the diagonal deformation of the specimen, resistance strain gauges were attached to the longitudinal bars, stirrups, and steel plate of the coupling beam.

## 3. Experimental Process and Failure Characteristics Analysis

### *3.1. Experimental Phenomena*

Steel plate–conventional concrete composite coupling beams with a small span-to-depth ratio [22–24]: For conventional concrete specimens (PRC-CB1, PRC-CB2, PRC-CB3, PRC-CB6, PRC-CB7, PRC-NS1, CB-1.5, and CB-2.5), diagonal cracks first appeared in the middle of the web when the load reached a certain level. As loading progressed, inclined cracks appeared in the tensile zone and propagated. With further load increase, diagonal cracks extended toward both ends until reaching the interface between the web and the upper end block, forming a major diagonal crack. These cracks continued to widen, and numerous small cracks emerged nearby. The shear diagonal crack eventually became the dominant one, nearly penetrating the entire web. Subsequently, the components entered the displacement control stage, the specimens reached the peak load under forward loading, the cracks of the specimens intensified, and the cracks of the concrete made obvious crackling sounds. Subsequently, with an increase in displacement, the crack width of the specimens increased under cyclic loads, and the web of the coupling beams was divided into many rhombic blocks by diagonal cracks staggered in two directions, and falling residue and spalling of the concrete at the infall occurred. In the process of repeated loading inside the specimen, a "dong dong" sound was constantly emitted. The specimen gradually lost its bearing capacity, and the test load ended. The failure morphology of each specimen is shown in Figure 3d–k.

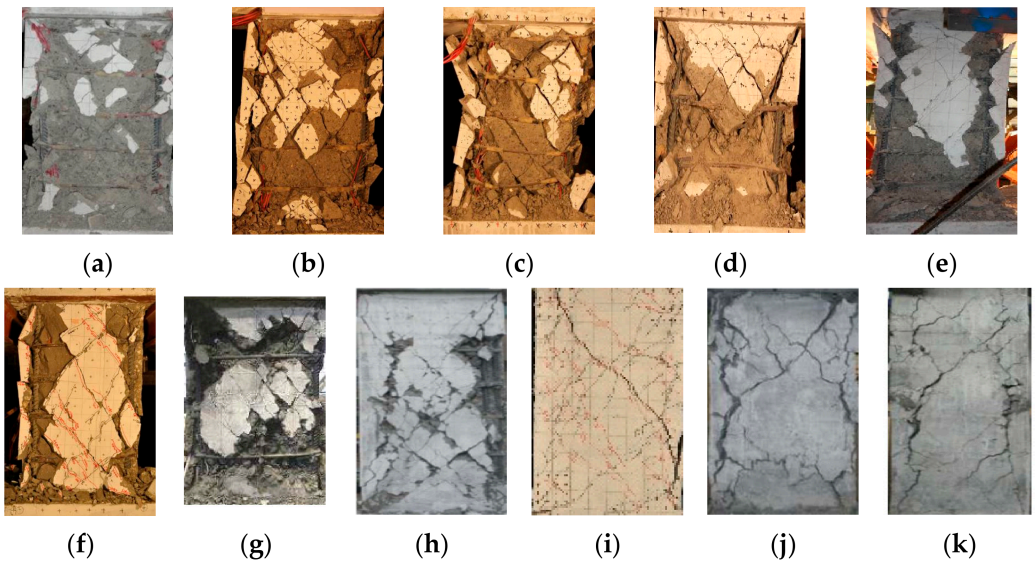



**Figure 3.** Failure mode of specimens. (**a**) PRC-CB1; (**b**) PRC-CB2; (**c**) PRC-CB3; (**d**) PRC-CB6; (**e**) PRC-CB7; (**f**) PRC-NS1; (**g**) CB-1.5 [22]; (**h**) CB-2.5 [22]; (**i**) PRCB-2; (**j**) DB-1.5 [22]; (**k**) DB-2.5 [22].

For steel plate–fiber-reinforced concrete composite coupling beams with a small span-to-depth ratio [22,25], when the specimens PRCB-2, DB-1.5, and DB-2.5 were loaded beyond

a certain value, diagonal cracks appeared in the beam. As the load increased, these fractures propagated toward the coupling beam's central to varying degrees. With continued loading, the diagonal cracks extended further, exhibiting a tendency toward a transfixion trend. At this stage, multi-strip small diagonal cracks formed, leading to the development of main diagonal cracks, and the coupling beam specimens began to yield. When the displacement loading reached a certain value, the coupling beam attained its peak load, causing the longitudinal rib and internal steel plate to yield, while numerous fibers within the matrix ruptured. Once concrete scaling or slippage occurred in the coupling beam specimen, further loading became inappropriate. Due to the bridging action of the fibers, the width of the diagonal cracks was effectively controlled at each loading stage. The failure morphology of each specimen is illustrated in Figure 3a–c.

### *3.2. Analysis of Failure Mode*

The equivalent yield point was determined using the equal energy method. This method replaces the actual curve with an ideal elastic–plastic polyline. The area enclosed by the polyline and the coordinate axes was set equal to that enclosed by the actual curve. The failure point was defined based on the peak load. When the load capacity of the specimen dropped to 85% of the peak load, the specimen was considered to have reached the failure state.

The ductility coefficient [27] was calculated using the following formula:

$$\overline{\mu} = \left(\left|\Delta_u^+\right| + \left|\Delta_u^-\right|\right) / \left(\left|\Delta_y^+\right| + \left|\Delta_y^-\right|\right)$$

where $\Delta_y$ is the yield displacement, and $\Delta_u$ is the ultimate displacement.

Based on the hysteretic curves of each specimen in Figure 4 and the data of feature points in Table 2, the following conclusions can be drawn.

**Table 2.** Experimental results of feature points of each specimen.

| Specimen | Loading Direction | Yield Point | | | Peak Point | | | Failure Point | | | Displacement Ductility Coefficient |
|---|---|---|---|---|---|---|---|---|---|---|---|
| | | $V_y$/kN | $\Delta_y$/mm | $\theta_y$ | $V_m$/kN | $\Delta_m$/mm | $\theta_m$ | $V_u$/kN | $\Delta_u$/mm | $\theta_u$ | $\overline{\mu}$ |
| PRC-NS1 | Positive | 405.85 | 4.71 | 1/102 | 455.52 | 9.89 | 1/49 | 387.19 | 19.9 | 1/24 | 4.02 |
| | Negative | 393.62 | 4.58 | 1/105 | 444.56 | 9.97 | 1/48 | 377.87 | 17.41 | 1/28 | |
| PRC-CB1 | Positive | 526.98 | 2.40 | 1/219 | 586.60 | 3.05 | 1/172 | 498.61 | 6.57 | 1/80 | 3.61 |
| | Negative | 435.17 | 3.06 | 1/172 | 493.30 | 6.89 | 1/76 | 419.31 | 13.12 | 1/40 | |
| PRC-CB2 | Positive | 571.45 | 2.51 | 1/209 | 638.00 | 3.22 | 1/163 | 542.30 | 7.03 | 1/75 | 3.36 |
| | Negative | 485.28 | 3.66 | 1/143 | 536.53 | 8.81 | 1/60 | 456.05 | 13.72 | 1/38 | |
| PRC-CB3 | Positive | 570.55 | 2.68 | 1/196 | 656.60 | 3.38 | 1/156 | 558.11 | 6.16 | 1/85 | 2.58 |
| | Negative | 454.35 | 4.19 | 1/125 | 528.95 | 6.90 | 1/76 | 449.60 | 11.56 | 1/45 | |
| PRC-CB6 | Positive | 668.80 | 3.46 | 1/93 | 741.50 | 4.76 | 1/67 | 630.28 | 8.54 | 1/37 | 2.26 |
| | Negative | 552.13 | 3.75 | 1/85 | 659.98 | 5.70 | 1/56 | 560.99 | 7.76 | 1/41 | |
| PRC-CB7 | Positive | 516.49 | 5.55 | 1/126 | 583.49 | 6.77 | 1/103 | 495.97 | 18.96 | 1/37 | 3.44 |
| | Negative | 471.47 | 5.83 | 1/120 | 521.67 | 8.54 | 1/82 | 443.42 | 20.24 | 1/35 | |
| CB-1.5 | Positive | 373.50 | 10.27 | 1/58 | 430.37 | 16.05 | 1/37 | 365.81 | 23.51 | 1/26 | 2.45 |
| | Negative | −355.52 | −8.97 | −1/67 | −395.87 | −17.18 | −1/35 | −336.49 | −23.75 | −1/25 | |
| CB-2.5 | Positive | 349.95 | 15.71 | 1/64 | 377.50 | 21.50 | 1/47 | 320.88 | 30.98 | 1/32 | 2.09 |
| | Negative | −310.07 | −13.95 | −1/72 | −344.81 | −24.09 | −1/42 | −293.09 | −30.71 | −1/33 | |
| PRCB-2 | Positive | 428.57 | 4.71 | 1/102 | 470.71 | 6.33 | 1/7640 | 400.10 | 12.83 | 1/38 | 2.78 |
| | Negative | 318.29 | 5.99 | 1/81 | 380.11 | 9.93 | 1/4932 | 323.10 | 16.94 | 1/29 | |
| DB-1.5 | Positive | 393.56 | 13.05 | 1/46 | 455.50 | 19.70 | 1/30 | 387.18 | 32.02 | 1/19 | 2.92 |
| | Negative | −355.96 | −10.38 | −1/58 | −402.03 | −19.50 | −1/31 | −341.73 | −34.35 | −1/17 | |
| DB-2.5 | Positive | 344.34 | 17.97 | 1/56 | 393.38 | 24.00 | 1/41 | 334.37 | 33.69 | 1/30 | 1.92 |
| | Negative | −331.94 | −15.92 | −1/63 | −361.71 | −23.95 | −1/41 | −307.45 | −31.23 | 1/32 | |

(1) Under cyclic loading, the steel plates at the beam–wall junction experienced varying degrees of tearing. Based on the maximum crack length observed in the specimens, fiber-reinforced concrete enhanced the mechanical properties of the embedded steel plates more effectively than conventional concrete. In addition, fiber-reinforced concrete and the embedded steel plates exhibited superior cooperative performance. Deformation and

cracking of the steel plates were primarily concentrated at the corners of the coupling beam, which also corresponded to the areas where concrete crushing was most severe.

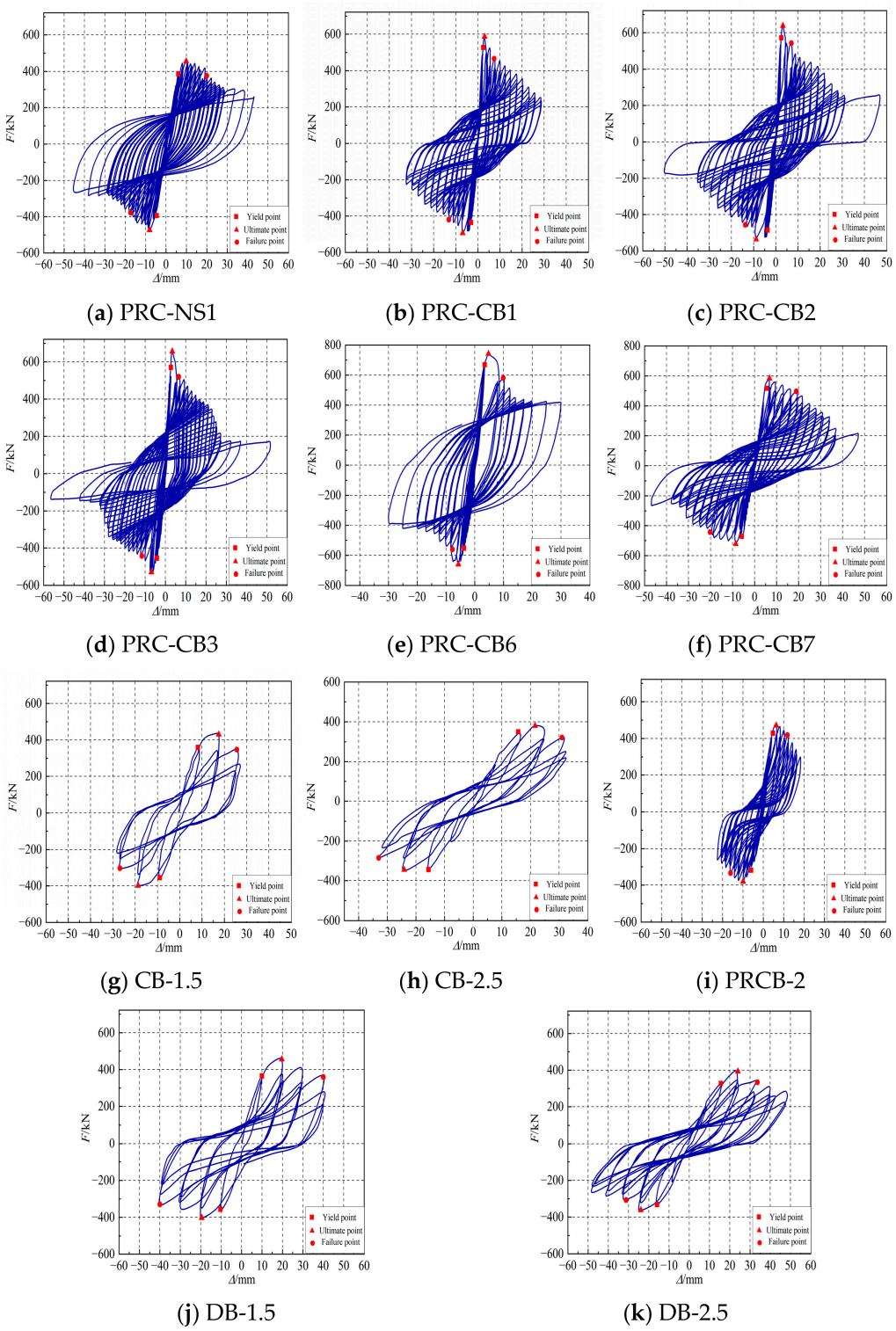



**Figure 4.** Hysteresis curve of each specimen.

(2) Due to the high load magnitude, particularly the combined effects of compressive and shear stresses induced by bending, local bending of the steel plate occurred at the junction of the wall limb and the tie beam. The buckling of the steel plate in the PRC coupling beams was more serious compared to that in beams with larger span-to-depth ratios.

## 4. Selected Restoring Force Model and Hysteresis Rules

### *4.1. Selected Restoring Force Model*

Due to the presence of the embedded steel plate, the overall stiffness of the steel plate–concrete composite coupling beam with a small span-to-depth ratio is significantly higher than that of an ordinary reinforced concrete coupling beam. However, stiffness degradation was still observed experimentally.

The number of test samples is limited. Introducing more parameters would lead to overfitting and reduce the generalization capability of the model. The trilinear model has fewer parameters and high robustness, making it more suitable for the current data scale. This choice prioritizes modeling simplicity over predictive accuracy, especially in the nonlinear elastic–plastic transition region where predictive accuracy is lower than that of higher-order alternatives.

Thus, in the restoring force model, a trilinear model is used to describe the skeleton curve of the steel plate–concrete composite coupling beam with a small span-to-depth ratio. The elasticity phase (OA) corresponds to the working state before beam cracking, and its slope reflects the initial stiffness. The yield point (A) roughly corresponds to the full development of major diagonal cracks and the first yielding of longitudinal reinforcement. The elastic–plastic stage (AB) corresponds to gradual yielding of the steel plate and its contribution to shear resistance. The peak point (B) corresponds to concrete crushing and large-scale yielding of the steel plate. The decline phase (BC) corresponds to intensified steel plate buckling and the resulting loss of load capacity. The OA segment represents the elasticity phase, during which the bearing capacity of the coupling beam reaches the yield load. The AB segment corresponds to the elastic–plastic stage, where the bearing capacity exceeds the yield load and reaches the peak load. The BC segment represents the decline phase, during which the bearing capacity decreases from the peak load to 85% of the peak load. Thus, the skeleton curve of the restoring force model adopts a trilinear model, as illustrated in Figure 5.

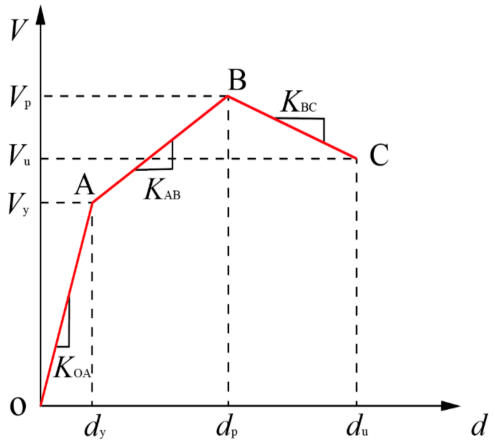



**Figure 5.** Trilinear model.

Through normalization (using $V/V_p$ and $\Delta/\Delta_u$ as coordinates), the skeleton curves of different specimens tend to converge. This means that the design parameters mainly affect the scaling factors required for normalization, rather than the normalized shape of the skeleton curve. Therefore, a detailed parametric sensitivity analysis is beyond the scope of this study and deferred to future work with more data.

### *4.2. Restoring Force Model Hysteresis Rules*

Under cyclic loads, the load stiffness of the specimens degraded to varying degrees at each stage. Therefore, based on the restoring force skeleton curve, linear regression was performed on the load stiffness of the specimens PRCB-2 [25], DB-1.5 [22], DB-2.5 [22], PRHTC-1.0 and PRHTC-2.0 from [28] and PRHTC-8t, PRHTC-10t, and PRHTC-12t from [12] under identical loading conditions. This analysis yielded the load stiffness of the steel plate–concrete composite coupling beams with a small span-to-depth ratio. Regarding unloading stiffness, two scenarios were considered: unloading stiffness without accounting for stiffness degradation and unloading stiffness incorporating stiffness degradation. Due to the presence of embedded steel plates in the composite coupling beams, the overall stiffness of these coupling beams is higher than that of conventional reinforced concrete (RC) coupling beams. The available samples are limited. Introducing more stiffness degradation parameters would cause overfitting and reduce the model's generalization capability and engineering practicality. Consequently, the unloading stiffness without considering stiffness degradation was adopted in the hysteretic rule of the restoring force model. It should be clearly stated that this simplified assumption makes the model unsuitable for detailed nonlinear cyclic analyses involving cumulative damage. The model is intended primarily for simplified engineering estimation, such as pushover analysis or preliminary seismic demand assessment.

Figure 6 illustrates the hysteretic rule of the restoring force model. The loading and unloading rules in the first and third quadrants are identical; therefore, only the rules for the first quadrant are described here. The OA stage represents the elasticity phase, where the load and unloading stiffness corresponds to the slope of the skeleton curve fitting equation, denoted as $K_{OA}$. Once the displacement exceeds the specimen's yield displacement, it enters the elastic–plastic stage (AB stage). The loading path begins at the origin (*O*) and end point at point a, with the load at point a determined using the skeleton curve fitting equation for the AB stage. The unloading path follows ac, maintaining a stiffness of $K_{OA}$. When the displacement reaches the peak displacement, the specimen enters the decline phase (BC stage). Here, the loading path starts from d′ and follows d′b, with the load at point b calculated using the skeleton curve fitting equation for the BC stage. The unloading stiffness remains $K_{OA}$. Additionally, in the hysteretic rule of the restoring force model, points a and b represent generalized displacement points in the elastic–plastic and decline phase, respectively. The specific number of loading cycles for each phase should be determined based on the test's hysteretic curve.

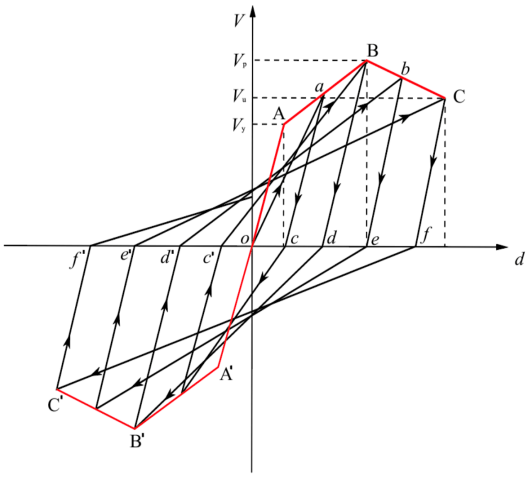



**Figure 6.** Hysteresis rules of restoring curve.

## 5. Restoring Force Model for Steel Plate–Conventional Concrete Composite Coupling Beams with Small Span-to-Depth Ratios

### *5.1. Restoring Force Model Skeleton Curve Fitting*

First, the test data for the specimens CB-1.5 and CB-2.5 from the literature [22], along with the specimens PRC-CB1, PRC-CB2, PRC-CB3, PRC-CB6, PRC-CB7, and PRC-NS1, were normalized. The test cost is high, and specimen fabrication is complex. The sample size is small. The dimensionless normalization procedure can mitigate, to some extent, the data dispersion caused by the insufficient sample size. To facilitate a more intuitive comparison between the calculated and experimental values using the trilinear model, only the load–displacement curve corresponding to 85% of the peak load is presented for skeleton curve comparison. Figure 7 illustrates the dimensionless skeleton curves of each specimen, where the horizontal scale represents the ratio of displacement to ultimate displacement ($\Delta/\Delta_u$), with $\Delta$ denoting the specimen's displacement and $\Delta_u$ representing the displacement at which the load decreases to 85% of the peak load. The vertical scale represents the ratio of load to peak load ($V/V_P$), where V is the applied load, and $V_P$ is the peak load of the specimen.

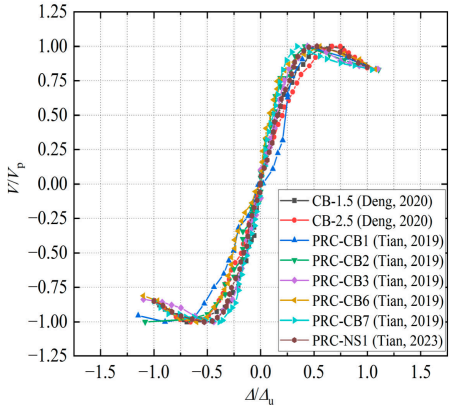
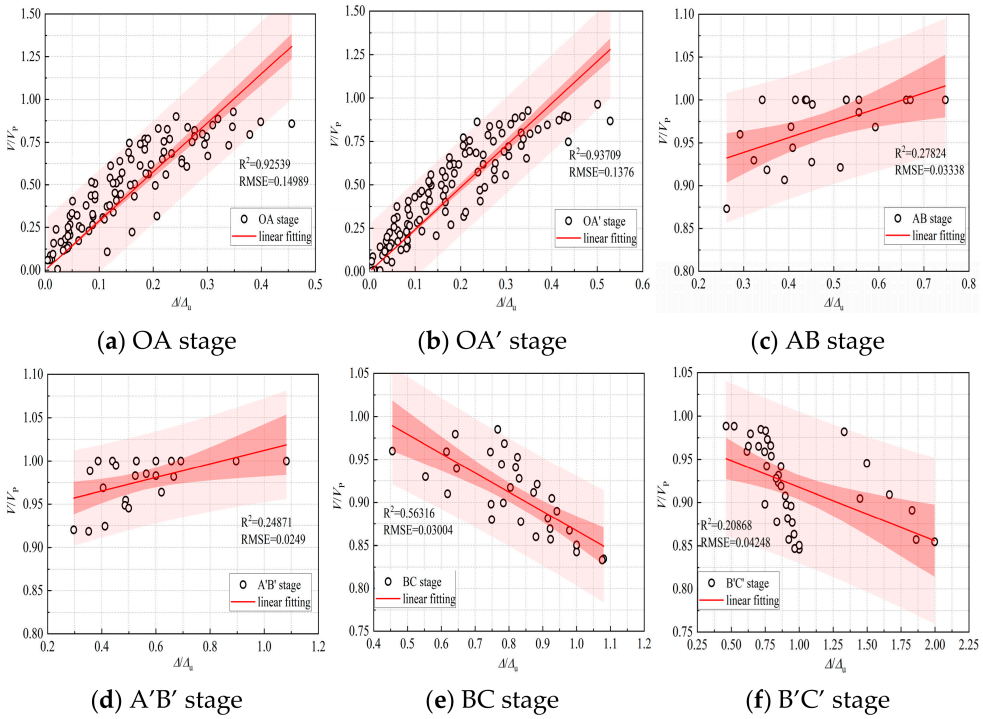



**Figure 7.** Dimensionless skeleton force model [22–24].

This study establishes a preliminary recovery force model based on existing data. The model is for steel plate–ordinary concrete composite coupling beams. The beams have a span-to-depth ratio of 0.9 to 2.5 and a plate ratio of 3% to 5%. Linear fitting was performed for each specimen as shown in Figure 8. Residual analysis plots are shown in Figure 9. The fitting includes the elasticity phase (positive OA stage and negative OA' stage). It also includes the elastic–plastic stage (positive AB stage and negative A'B' stage). It also includes the decline phase (positive BC stage and negative B'C' stage). The linear fitting process involved compiling data points from the normalized skeleton curves of different specimens at each stage and subsequently performing linear fitting. Table 3 presents the fitting equations for steel plate–conventional concrete composite coupling beams with a small span-to-depth ratio at various loading stages. The fitting accuracy varies by stage: high in the elastic stages (OA and OA', $R^2 > 0.92$), low in the elastic–plastic stages (AB: $R^2 \approx 0.28$, A'B': $R^2 \approx 0.25$), and moderate in BC ($R^2 \approx 0.56$) but low in B'C' ($R^2 \approx 0.21$). The lower $R^2$ values in the negative loading branches (A'B' and B'C') may be attributed to experimental asymmetry, although the exact causes were not further investigated.

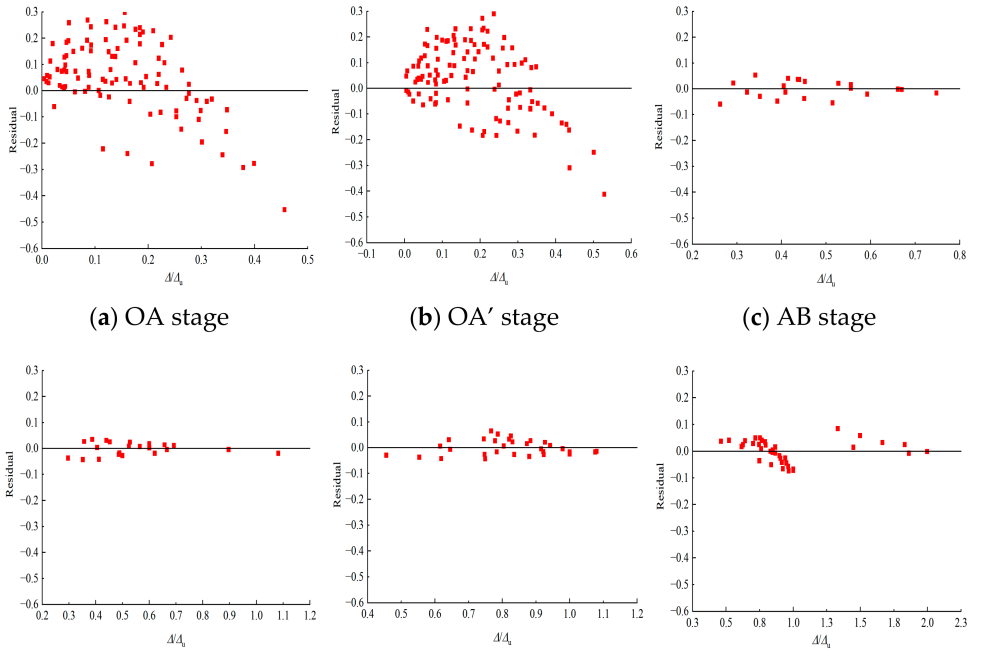
The above fitting equations are primarily applicable within the following parameter ranges: span-to-depth ratio of 0.9~2.5, plate ratio of 3~5%, concrete strength of C30~C50, longitudinal reinforcement ratio of 0.86~2.23%, stirrup ratio of 0.56~0.63%, and steel plate thickness of 6~10 mm. For configurations significantly outside these ranges, additional experimental validation is required to verify applicability.




(**a**) OA stage (**b**) OA′ stage (**c**) AB stage

(**d**) A′B′ stage (**e**) BC stage (**f**) B′C′ stage

**Figure 8.** Skeleton curve fitting diagram of each stage.




(**a**) OA stage (**b**) OA′ stage (**c**) AB stage

(**d**) A′B′ stage (**e**) BC stage (**f**) B′C′ stage

**Figure 9.** Residual analysis of each stage.

**Table 3.** Skeleton curve fitting equation and slope of each stage.

| Stage | Fitting Equation | Slope | $R^2$ | RMSE | Lower 95% CI | Upper 95% CI |
|---|---|---|---|---|---|---|
| OA | $V/V_P = 2.87264\ \Delta/\Delta_u$ | 2.87264 | 0.92539 | 0.14989 | 2.70917 | 3.03611 |
| OA′ | $V/V_P = 2.42159\ \Delta/\Delta_u$ | 2.42159 | 0.93709 | 0.1376 | 2.30247 | 2.5407 |
| AB | $V/V_P = 0.17290\ \Delta/\Delta_u + 0.88702$ | 0.17290 | 0.27824 | 0.03338 | 0.05331 | 0.29248 |
| A′B′ | $V/V_P = 0.07854\ \Delta/\Delta_u + 0.93376$ | 0.07854 | 0.24871 | 0.0249 | 0.01659 | 0.01659 |
| BC | $V/V_P = -0.22427\ \Delta/\Delta_u + 1.09137$ | −0.22427 | 0.56316 | 0.03004 | −0.29792 | −0.15062 |
| B′C′ | $V/V_P = -0.06193\ \Delta/\Delta_u + 0.97943$ | −0.06193 | 0.20868 | 0.04248 | −0.10022 | −0.02363 |

Figure 10 compares the experimental and calculated value skeleton curves for each specimen. The results indicate that the trilinear model reasonably captures the displacement and load at the feature points of the steel plate–conventional concrete composite coupling beams with a small span-to-depth ratio. Additionally, the discrepancy between the calculated and experimental values is minimal. However, this validation used the same dataset as that of model development. The reported performance may therefore overestimate the predictive capability for unseen specimens. Table 4 presents the absolute relative errors between the experimental and predicted load-carrying capacities at different characteristic points of the specimens.

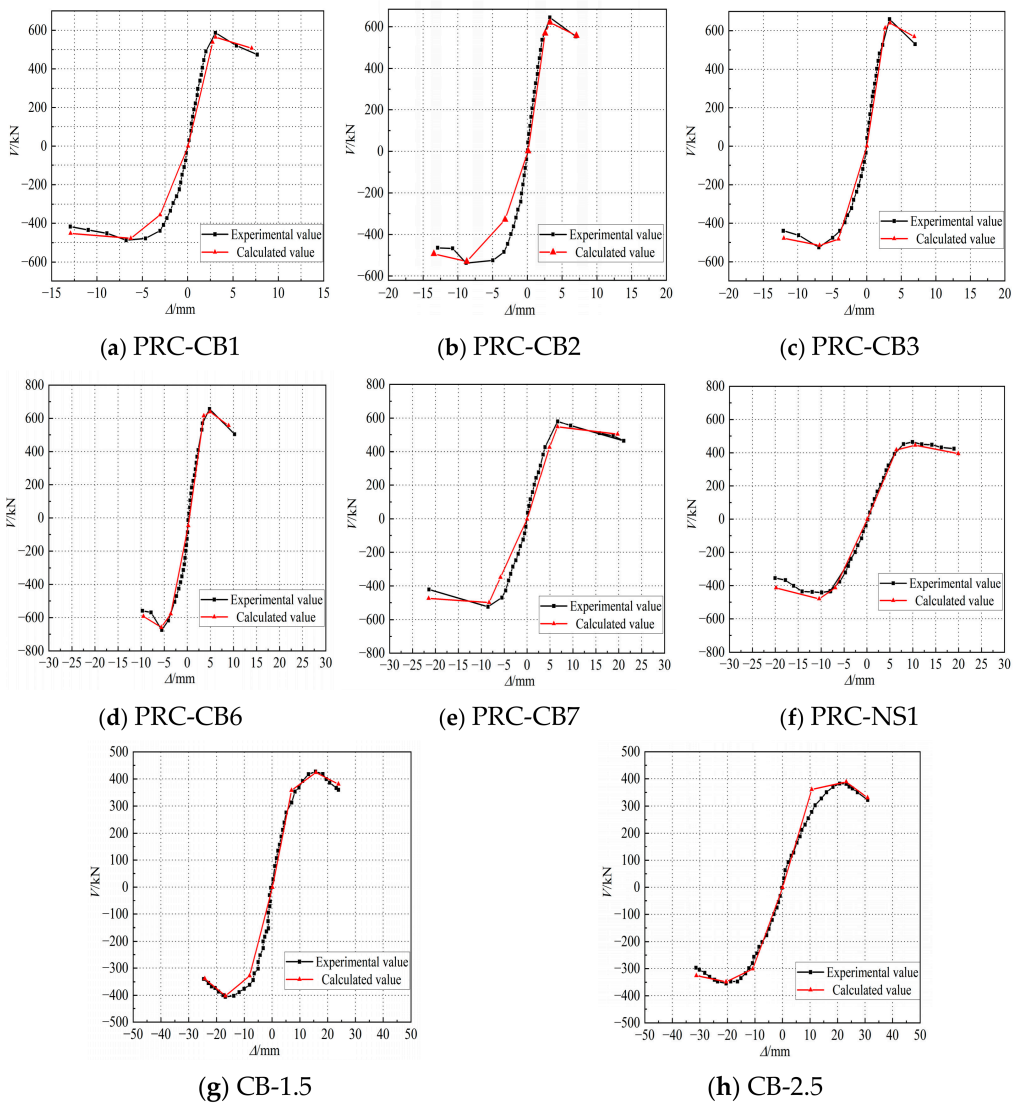



**Figure 10.** Comparison of skeleton curves of each specimen.

**Table 4.** Absolute relative errors at characteristic points.

| Specimen | Loading Direction | Yield Point | | | Peak Point | | | Failure Point | | |
|---|---|---|---|---|---|---|---|---|---|---|
| | | Test (kN) | Pred. (kN) | Error (%) | Test (kN) | Pred. (kN) | Error (%) | Test (kN) | Pred. (kN) | Error (%) |
| CB-1.5 | Positive | 364.03 | 357.59 | −1.8 | 422.03 | 422.59 | 0.1 | 358.73 | 380.14 | 6 |
| | Negative | 359.15 | 327.82 | −8.7 | 403.45 | 398.65 | −1.2 | 342.93 | 340.63 | −0.7 |
| CB-2.5 | Positive | 328.25 | 359.54 | 9.5 | 380.24 | 388.22 | 2.1 | 323.2 | 329.71 | 2 |
| | Negative | 316.42 | 298.92 | −5.5 | 350.3 | 345.17 | −1.5 | 297.75 | 321.4 | 7.9 |

**Table 4.** *Cont.*

| Specimen | Loading Direction | Yield Point | | | Peak Point | | | Failure Point | | |
|---|---|---|---|---|---|---|---|---|---|---|
| | | Test (kN) | Pred. (kN) | Error (%) | Test (kN) | Pred. (kN) | Error (%) | Test (kN) | Pred. (kN) | Error (%) |
| PRC-CB1 | Positive | 526.98 | 539.23 | 2.3 | 586.6 | 564.44 | −3.8 | 498.61 | 508.64 | 2 |
| | Negative | 435.17 | 358.37 | −17.6 | 493.3 | 481.14 | −2.5 | 419.31 | 452.61 | 7.9 |
| PRC-CB2 | Positive | 571.45 | 568.15 | −0.6 | 638 | 616.58 | −3.4 | 542.3 | 553.21 | 2 |
| | Negative | 476.28 | 324.81 | −31.8 | 536.53 | 528.49 | −1.5 | 456.05 | 492.26 | 7.9 |
| PRC-CB3 | Positive | 570.55 | 613.9 | 7.6 | 656.6 | 638.11 | −2.8 | 558.11 | 569.34 | 2 |
| | Negative | 454.35 | 486.74 | 7.1 | 528.95 | 518.4 | −2 | 449.6 | 485.31 | 7.9 |
| PRC-CB6 | Positive | 668.8 | 702.92 | 5.1 | 741.5 | 727.56 | −1.9 | 630.28 | 642.95 | 2 |
| | Negative | 552.13 | 559.37 | 1.3 | 659.98 | 646.63 | −2 | 560.99 | 572.27 | 2 |
| PRC-CB7 | Positive | 530.03 | 427.75 | −19.3 | 583.94 | 552.41 | −5.4 | 496.35 | 506.34 | 2 |
| | Negative | 459.45 | 343.7 | −25.2 | 510.54 | 492.23 | −3.6 | 433.96 | 468.42 | 7.9 |
| PRC-NS1 | Positive | 382.68 | 416.61 | 8.9 | 450.21 | 444.91 | −1.2 | 418.47 | 394.23 | −5.8 |
| | Negative | 382.68 | 413.91 | 8.2 | 450.21 | 480.11 | 6.6 | 419.01 | 413.91 | −1.2 |

### *5.2. Verification of Restoring Force Model*

Figure 11 compares the calculated and observed values obtained from the restoring force model for steel plate–conventional concrete composite coupling beams with a small span-to-depth ratio. The results demonstrate that the calculation model effectively captures the hysteretic response of the composite coupling beams under cyclic loads, indicating a reasonable level of the restoring force model. However, for the specimens PRC-CB7 and PRC-NS1, deviations between the calculated and experimental values are observed during the load decline phase, particularly in the positive and negative loading directions. These cases may have arisen from experimental factors such as bolt loosening or ideal boundary conditions, which can lead to deviations in the positive and negative hysteretic curves. Consequently, some deviations between the calculated and experimental values are expected. However, the same dataset was used for both model development and validation. This may overestimate the predictive capability for unseen specimens.

Table 5 presents the experimental and predicted energy dissipation at the yield, peak and failure points for all specimens, along with the corresponding relative errors. For ordinary concrete coupling beams, most absolute relative errors are within 10%, with the highest accuracy observed at the peak point (mean absolute relative error of about 5%). A slightly larger error (36%) occurs for the specimen CB-2.5 at the failure point.

**Table 5.** Absolute relative errors of hysteretic energy dissipation.

| Specimen | Yield Point | | | Peak Point | | | Failure Point | | |
|---|---|---|---|---|---|---|---|---|---|
| | Test (kN·mm) | Pred. (kN·mm) | Error (%) | Test (kN·mm) | Pred. (kN·mm) | Error (%) | Test (kN·mm) | Pred. (kN·mm) | Error (%) |
| CB-1.5 | 2583.99 | 3057.59 | 18 | 9707.42 | 10,022.59 | 3 | 11,492.19 | 12,168.38 | 6 |
| CB-2.5 | 3349.24 | 3662.54 | 9 | 7598.27 | 6723.07 | 12 | 7300.54 | 9895.85 | 36 |
| PRC-CB1 | 2761.30 | 2192.72 | 21 | 3452.81 | 3699.91 | 7 | 5301.02 | 5728.71 | 8 |
| PRC-CB2 | 1072.50 | 975.40 | 9 | 4665.47 | 5026.65 | 8 | 5589.75 | 5978.85 | 7 |
| PRC-CB3 | 776.10 | 643.70 | 17 | 6117.23 | 4555.51 | 26 | 6328.66 | 6720.11 | 6 |
| PRC-CB6 | 2060.16 | 1777.58 | 14 | 8032.28 | 7531.44 | 6 | 7937.26 | 7245.86 | 9 |
| PRC-CB7 | 485.41 | 438.05 | 10 | 2388.17 | 2525.57 | 6 | 11,288.21 | 12,184.58 | 8 |
| PRC-NS1 | 569.69 | 457.61 | 20 | 3218.25 | 2778.84 | 14 | 8268.81 | 9700.87 | 17 |

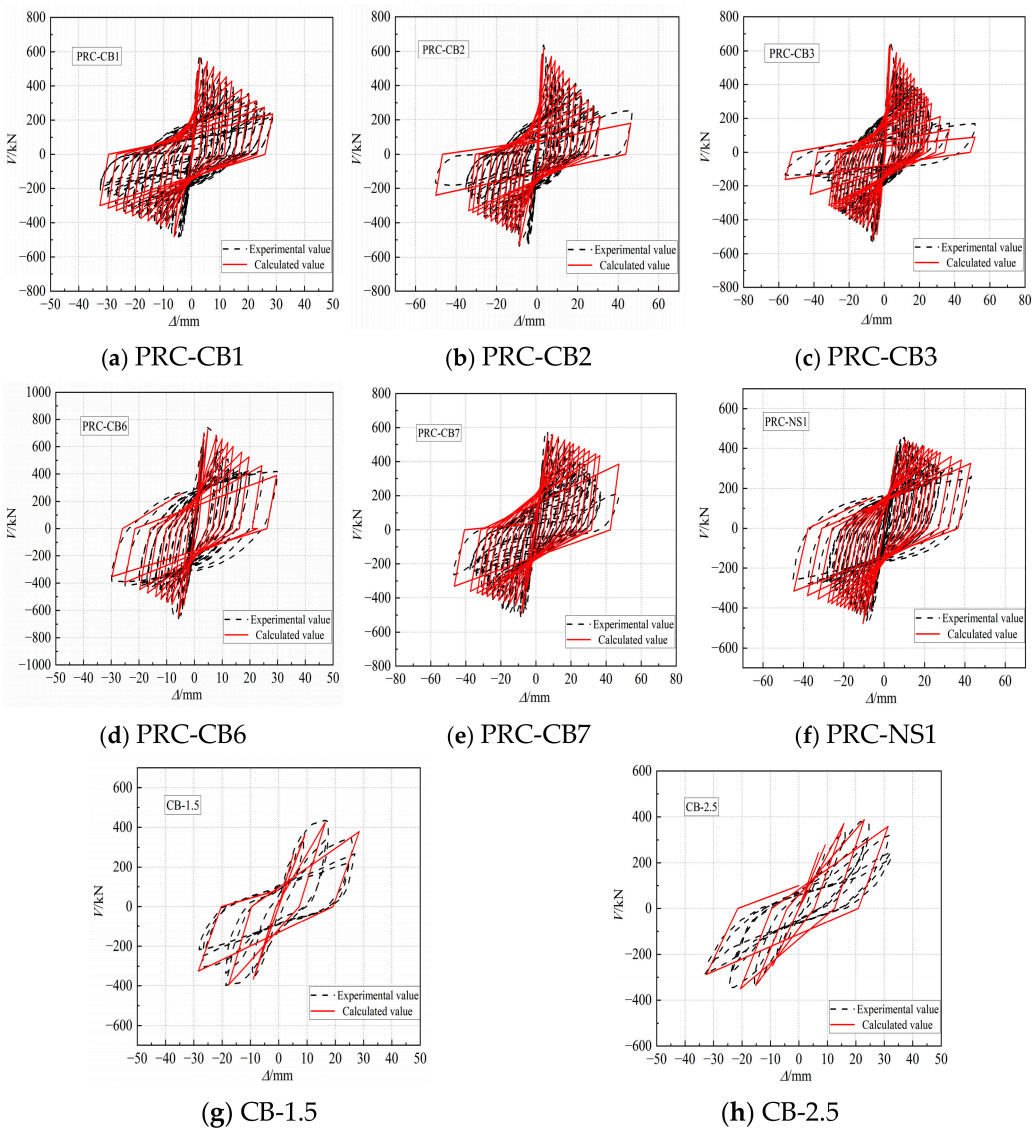



**Figure 11.** Comparison of the restoring force curves of each specimen.

## 6. Restoring Force Model for Steel Plate–Fiber-Reinforced Concrete Composite Coupling Beams with Small Span-to-Depth Ratio

### *6.1. Restoring Force Model Skeleton Curve Fitting*

To establish the restoring force model for steel plate–fiber-reinforced concrete composite coupling beams with a small span-to-depth ratio, dimensionless skeleton curves were derived for the test specimens PRCB-2, DB-1.5, and DB-2.5. The dimensionless skeleton curves for each specimen are shown in Figure 12. The horizontal scale represents the ratio of displacement to ultimate displacement ($\Delta/\Delta_u$), where $\Delta$ is the displacement of the specimen, and $\Delta_u$ is the displacement corresponding to the load dropping to 85% of the peak load. The vertical scale represents the ratio of load to peak load ($V/V_P$), where V is the load of the specimen, and $V_P$ is the peak load.

To describe the skeleton curves of the steel plate–fiber-reinforced concrete composite coupling beams with a small span-to-depth ratio within the tested parameter ranges, the skeleton curves of the PRCB-2, DB-1.5 and DB-2.5 specimens at each stage were fitted respectively. As shown in Figure 13, the OA stage was the forward loading elasticity phase, and the OA' stage was the negative loading elasticity phase. The AB stage is the elastic–plastic stage under forward loading, the A'B' stage is the elastic–plastic stage under

negative loading, the BC stage is the decline phase under forward loading, and the B′C′ stage is the decline phase under negative loading. Table 6 shows the fitting equations and stiffness of the skeleton curve at each stage. For the steel plate–fiber-reinforced concrete composite coupling beams with a small span-to-depth ratio, the fitting accuracy is high in the elastic stages (OA: $R^2$ = 0.90, OA′: $R^2$ = 0.93) and in the decline stages (BC: $R^2$ = 0.78, B′C′: $R^2$ = 0.83), and moderate in the elastic–plastic stages (AB: $R^2$ = 0.45, A′B′: $R^2$ = 0.58). The moderate $R^2$ values in the elastic–plastic stage are acceptable for engineering trend prediction. Residual analysis plots are shown in Figure 14. We illustrate this by comparing the slope differences between the two sets of fitting equations. The fiber-reinforced concrete beam shows a slightly higher slope in the elasticity phase and a gentler slope in the decline phase. This behavior is consistent with the fiber bridging effect. The fiber bridging effect delays crack development and damage accumulation. The low fitting accuracy of the elastic–plastic stage is attributed to three factors: large specimen-to-specimen variations in steel plate buckling and concrete crushing, the limited sample size of only 11 specimens, and the increasing randomness of micro-damage such as fiber fracture and local buckling. Thus, this stage is suitable only for trend prediction, not for precise point estimation.

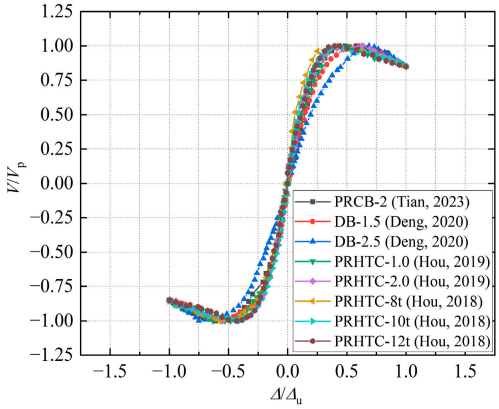
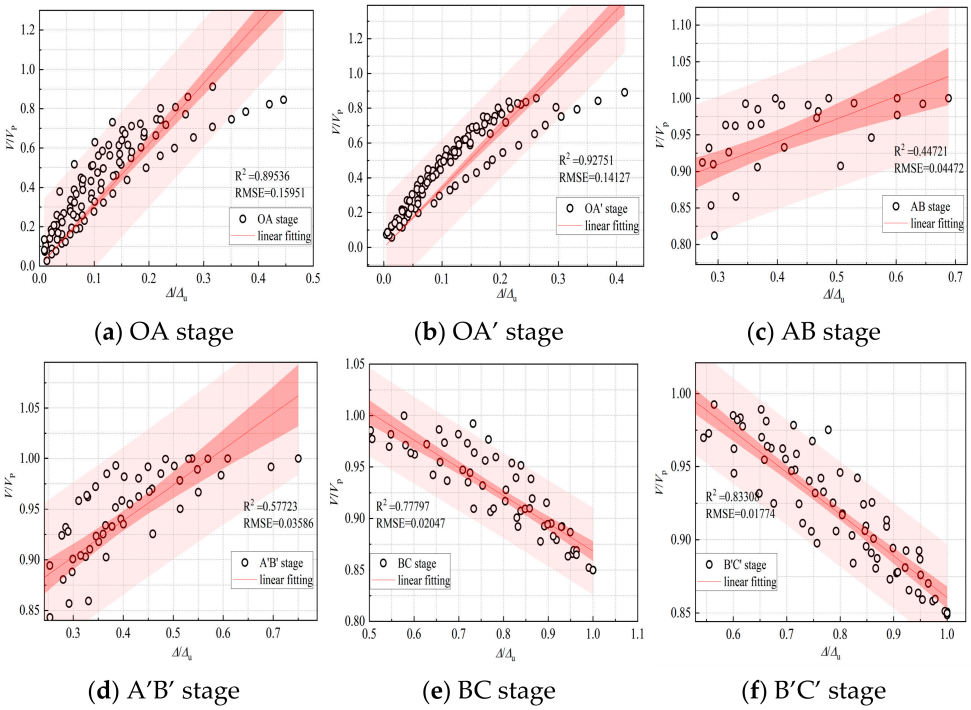



**Figure 12.** Dimensionless skeleton curve [12,22,25,28].



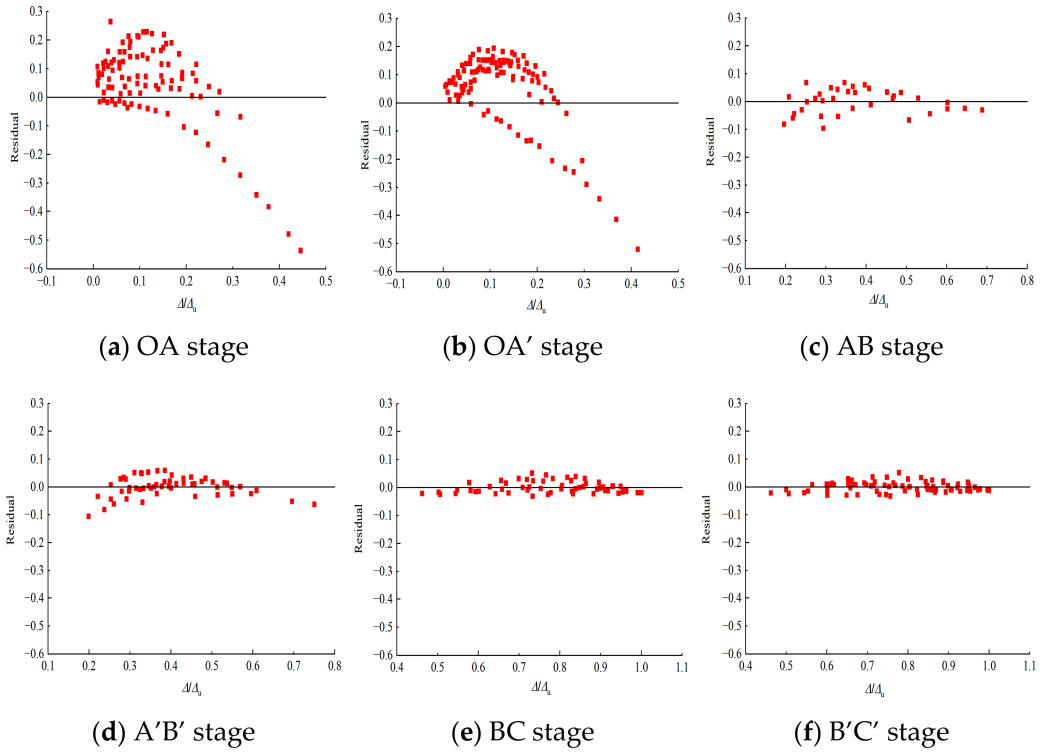

(**a**) OA stage (**b**) OA′ stage (**c**) AB stage

(**d**) A′B′ stage (**e**) BC stage (**f**) B′C′ stage

**Figure 13.** Skeleton curve fitting diagram of each stage.

**Table 6.** Skeleton curve fitting equation and slope of each stage.

| Stage | Fitting Equation | Slope | $R^2$ | RMSE | Lower 95% CI | Upper 95% CI |
|---|---|---|---|---|---|---|
| OA | $V/V_P = 3.09991\ \Delta/\Delta_u$ | 3.09991 | 0.89536 | 0.15951 | 2.89778 | 3.30204 |
| OA′ | $V/V_P = 3.41439\ \Delta/\Delta_u$ | 3.41439 | 0.92751 | 0.14127 | 3.22973 | 3.59904 |
| AB | $V/V_P = 0.30985\ \Delta/\Delta_u + 0.8166$ | 0.30985 | 0.44721 | 0.04472 | 0.19178 | 0.42792 |
| A′B′ | $V/V_P = 0.35377\ \Delta/\Delta_u + 0.79692$ | 0.35377 | 0.57723 | 0.03586 | 0.27169 | 0.43586 |
| BC | $V/V_P = -0.26971\ \Delta/\Delta_u + 1.13807$ | −0.26971 | 0.77797 | 0.02047 | −0.30717 | −0.23225 |
| B′C′ | $V/V_P = -0.28409\ \Delta/\Delta_u + 1.14477$ | −0.28409 | 0.83308 | 0.01774 | −0.31352 | −0.25467 |




(**a**) OA stage (**b**) OA′ stage (**c**) AB stage

(**d**) A′B′ stage (**e**) BC stage (**f**) B′C′ stage

**Figure 14.** Residual analysis of each stage.

Figure 15 compares the experimental and calculated values of the skeleton curves for each specimen. The results demonstrate that the trilinear model effectively predicts the skeleton curves of steel plate–fiber-reinforced concrete composite coupling beams with a small span-to-depth ratio, with minimal differences between the calculated and experimental values. This indicates that the mathematical model of the restoring force skeleton curve can effectively describe the behavior of steel plate–fiber-reinforced concrete composite coupling beams with a small span-to-depth ratio. However, the proposed model is a preliminary engineering approximation. Its applicability is limited to the following ranges: a span-to-depth ratio of 0.9~2.5, a plate ratio of 3~5%, concrete strength of C30~C50, a longitudinal reinforcement ratio of 0.86~2.23%, a stirrup ratio of 0.56~0.63%, and a steel plate thickness of 6~10 mm. Moreover, the same dataset was used for both model development and validation. This may overestimate the predictive capability for unseen specimens. Table 7 presents the absolute relative errors between the experimental and predicted load-carrying capacities at different characteristic points of the specimens.

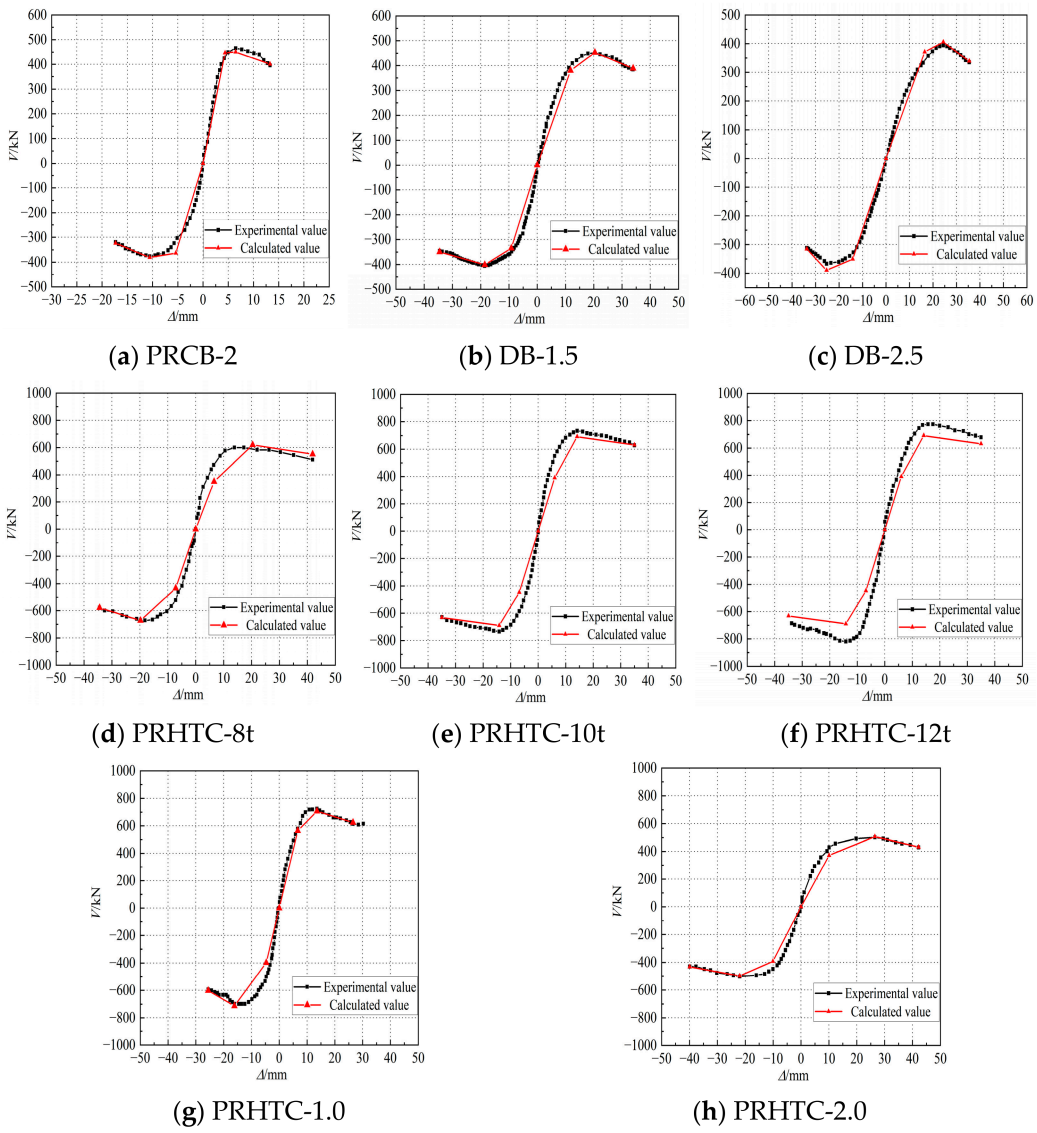


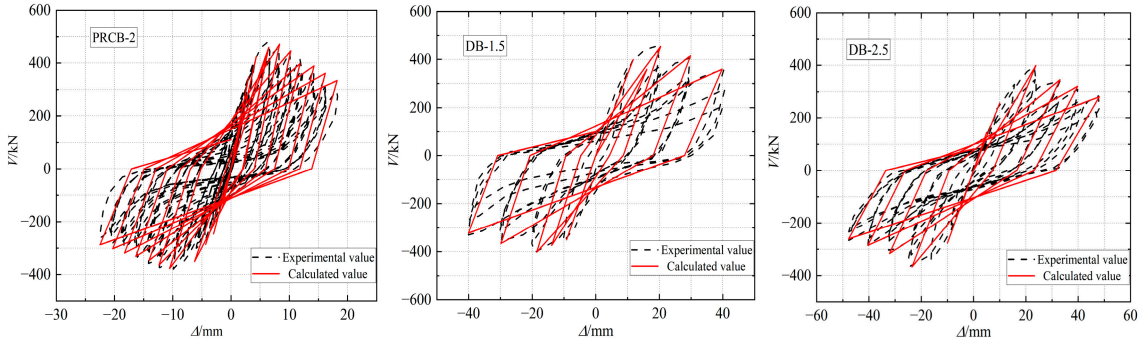

**Figure 15.** Comparison of skeleton curves of each specimen.

**Table 7.** Absolute relative errors at characteristic points.

| Specimen | Loading Direction | Yield Point | | | Peak Point | | | Failure Point | | |
|---|---|---|---|---|---|---|---|---|---|---|
| | | Test (kN) | Pred. (kN) | Error (%) | Test (kN) | Pred. (kN) | Error (%) | Test (kN) | Pred. (kN) | Error (%) |
| PRCB-2 | Positive | 430.23 | 447 | 3.9 | 465.77 | 450.56 | −3.3 | 395.9 | 400.88 | 1.3 |
| | Negative | 312.12 | 363.08 | 16.3 | 376.27 | 380.92 | 1.2 | 319.83 | 323.85 | 1.3 |
| DB-1.5 | Positive | 399.45 | 380 | −4.9 | 451.51 | 452.86 | 0.3 | 383.78 | 388.61 | 1.3 |
| | Negative | 350.29 | 334.31 | −4.6 | 406.06 | 400.81 | −1.3 | 345.15 | 349.49 | 1.3 |
| DB-2.5 | Positive | 341.02 | 370.91 | 8.8 | 393.94 | 405.69 | 3 | 334.85 | 339.06 | 1.3 |
| | Negative | 329.06 | 350.54 | 6.5 | 366.66 | 389.5 | 6.2 | 311.66 | 315.58 | 1.3 |
| PRHTC-1.0 | Positive | 579.12 | 564.37 | −2.5 | 725.21 | 707.08 | −2.5 | 616.43 | 624.18 | 1.3 |
| | Negative | 499.6 | 397.3 | −20.5 | 699 | 713.06 | 2 | 594.15 | 601.62 | 1.3 |
| PRHTC-2.0 | Positive | 429.38 | 371.6 | −13.5 | 501.7 | 507.36 | 1.1 | 426.44 | 431.8 | 1.3 |
| | Negative | 447.46 | 392.43 | −12.3 | 501.7 | 497.68 | −0.8 | 426.44 | 431.8 | 1.3 |
| PRHTC-8t | Positive | 472 | 351 | −25.6 | 641 | 620.23 | −3.2 | 510 | 551.7 | 8.2 |
| | Negative | 522.2 | 432.81 | −17.1 | 672.22 | 672.19 | 0 | 571.39 | 578.57 | 1.3 |
| PRHTC-10t | Positive | 551.08 | 390.34 | −29.2 | 733.85 | 691.36 | −5.8 | 623.77 | 631.61 | 1.3 |
| | Negative | 584.31 | 446.33 | −23.6 | 733.85 | 689.98 | −6 | 623.77 | 631.61 | 1.3 |
| PRHTC-12t | Positive | 551.08 | 390.34 | −29.2 | 733.85 | 691.36 | −5.8 | 623.77 | 631.61 | 1.3 |
| | Negative | 584.31 | 446.33 | −23.6 | 733.85 | 689.98 | −6 | 623.77 | 631.61 | 1.3 |

### *6.2. Verification of Restoring Force Model*

Figure 16 compares the calculated values from the restoring force model with the experimentally measured values for each specimen. As shown in Figure 16, the predicted hysteretic curves are in reasonable agreement with the experimental results, capturing key features such as peak loads and the overall loop shape. However, some discrepancies are observed in the unloading paths due to the assumption of constant unloading stiffness. Therefore, the model is suitable for trend prediction and pushover analysis, but not for high-precision simulation of detailed hysteresis loops.




(**a**) PRCB-2 (**b**) DB-1.5 (**c**) DB-2.5

**Figure 16.** Comparison of the restoring force curves of each specimen.

Table 8 presents the experimental and predicted energy dissipation at the yield, peak and failure points for all specimens, along with the corresponding relative errors.

**Table 8.** Absolute relative errors of hysteretic energy dissipation.

| Specimen | Yield Point | | | Peak Point | | | Failure Point | | |
|---|---|---|---|---|---|---|---|---|---|
| | Test (kN·mm) | Pred. (kN·mm) | Error (%) | Test (kN·mm) | Pred. (kN·mm) | Error (%) | Test (kN·mm) | Pred. (kN·mm) | Error (%) |
| PRCB-2 | 1006.48 | 1178.24 | 17 | 3847.48 | 3573.80 | 7 | 5258.09 | 4961.18 | 6 |
| DB-1.5 | 2514.74 | 3085.92 | 23 | 10,474.76 | 8281.52 | 21 | 11,956.73 | 14,145.82 | 18 |
| DB-2.5 | 3368.47 | 3700.91 | 10 | 8602.46 | 8122.38 | 6 | 9707.91 | 10,471.43 | 8 |

For fiber-reinforced concrete coupling beams, the three specimens show relative errors within 20%. It should be noted that the PRHTC-1.0, PRHTC-2.0, PRHTC-8t, PRHTC-10t, PRHTC-12t specimens were used only for skeleton curve fitting because their complete hysteresis loops were not available from the original publications; therefore, their hysteretic energy dissipation could not be extracted for comparison. Overall, the proposed model provides acceptable engineering accuracy for energy dissipation prediction.

The predictive uncertainty of the proposed restoring force model arises from several aspects. Material variability, such as differences in concrete strength and steel plate yield strength among specimens, affects the input parameters. Geometric deviations, including minor differences in specimen dimensions, lead to scattering in the normalized skeleton curves. Experimental uncertainties, such as loading misalignment, friction at supports, measurement noise, and idealization of boundary conditions, introduce discrepancies between measured and true responses. Model simplifications, including the use of a trilinear skeleton curve, the assumption of constant unloading stiffness, and the neglect of pinching effects, inherently limit the model's ability to capture all details of the cyclic response. The fitting equations of the proposed model are primarily applicable within the following ranges: a span-to-depth ratio of 0.9~2.5, a plate ratio of 3~5%, concrete strength

of C30~C50, a longitudinal reinforcement ratio of 0.86~2.23%, a stirrup ratio of 0.56~0.63%, and a steel plate thickness of 6~10 mm. For structural configurations significantly outside these ranges, additional experimental validation is required to verify applicability.

In summary, the proposed model should be regarded as an engineering-oriented preliminary restoring force model. Its main value lies in providing a simple and transparent empirical estimation tool for engineering practice. Due to high testing costs and complex specimen fabrication, the sample size is relatively limited. The reported goodness-of-fit metrics may therefore overestimate the model's predictive capability for unseen specimens. Independent validation using a separate dataset will be adopted in future work.

## 7. Conclusions

In this paper, based on experimental data and the literature, restoring force models for steel plate–conventional concrete composite coupling beams and steel plate–fiber-reinforced concrete composite coupling beams with a small span-to-depth ratio were established. The following conclusions were drawn:

(1) Fiber-reinforced concrete improves the failure mode of composite coupling beams and exhibits better synergy with the embedded steel plate than conventional concrete, leading to more effective utilization of the steel plate's mechanical properties.

(2) Based on dimensionless skeleton curves, trilinear fitting equations were developed for steel plate–ordinary concrete and steel plate–fiber-reinforced concrete coupling beams with small span-to-depth ratios.

(3) The predictive accuracy of the proposed models varies by stage: high in the elastic stage, moderate in the descending stage, and low in the elastic–plastic stage. The elastic–plastic stage is suitable only for trend prediction, particularly in the nonlinear transition region, and is not recommended for precise point estimation.

(4) The proposed model is a preliminary engineering approximation, not a generalized constitutive model. Its applicability is limited to steel plate–concrete composite coupling beams with a span-to-depth ratio of 0.9~2.5, a plate ratio of 3~5%, concrete strength of C30~C50, a longitudinal reinforcement ratio of 0.86~2.23%, a stirrup ratio of 0.56~0.63%, and a steel plate thickness of 6~10 mm. The proposed model adopts a simplified constant unloading stiffness assumption and does not account for the experimentally observed unloading stiffness degradation. Therefore, the model is not recommended for detailed nonlinear cyclic analysis involving cumulative damage and repeated loading. Instead, it is primarily suitable for simplified engineering estimation, such as pushover analysis or preliminary seismic demand assessment. The constant unloading stiffness assumption also leads to deviations in the shape of the hysteresis loops, particularly at large deformation stages. Incorporating a simplified stiffness degradation formulation is a key direction for future work.

(5) Compared with previous restoring force models for conventional RC or fiber-reinforced concrete coupling beams (without steel plates), the proposed model is specifically tailored to steel plate–concrete composite coupling beams. A direct quantitative comparison is not yet feasible due to differences in structural mechanisms. Future work will collect more experimental data and conduct systematic comparisons to further quantify the trade-offs between accuracy, simplicity, and applicability. In addition, a stiffness degradation formulation and more precise loading–unloading paths will be incorporated. This study has practical engineering value and provides a convenient and transparent empirical tool for estimating the restoring force characteristics of steel plate–concrete composite coupling beams.

(6) High testing costs and complex specimen fabrication have limited the sample size. The same dataset was used for both model development and validation, without an

independent dataset or cross-validation. The reported goodness-of-fit metrics may therefore overestimate the predictive capability for unseen specimens. Independent validation is the standard for assessing generalizability and is a necessary direction for future work. The proposed restoring force model can be implemented as follows: Input the peak load ($V_p$), the ultimate displacement ($\Delta_u$), and the matrix type. Select the corresponding trilinear skeleton coefficients, then scale the dimensionless skeleton curve by $V_p$ and $\Delta_u$ to obtain the actual load–displacement relationship. For each displacement increment, apply the following hysteresis rules: if loading, follow the skeleton curve; if unloading, use the constant elastic stiffness ($K_{OA}$) to unload linearly to zero load, and record the residual displacement; if reloading, draw a straight line from the residual displacement point back to the skeleton curve at the same displacement. Repeat this process until the target displacement or failure condition is reached. The resulting hysteretic curve can be used in pushover analysis for simplified engineering estimation. It is not recommended for detailed time–history analysis involving cumulative damage.

**Author Contributions:** Conceptualization, J.T.; Methodology, Y.M., X.M., Y.Q. and Y.Z.; Software, X.M.; Validation, Y.Q. and Y.Z.; Formal analysis, J.T.; Writing—review & editing, Y.M., Y.Q. and Y.Z.; Supervision, L.M. and H.L.; Project administration, L.M. and H.L.; Funding acquisition, Y.M. and J.T. All authors have read and agreed to the published version of the manuscript.

**Funding:** This study was supported by the Ningxia Natural Science Foundation (Grant No. 2023AAC03317), the Special Fund Project for Basic Scientific Research of Central Universities of North Minzu University (Grant No. 2025XYZTM01), and the Natural Science Basic Research Program in Shaanxi Province of China (Grant No. 2025JC-YBMS-449).

**Data Availability Statement:** The data presented in this study are available on request from the corresponding author. The data are not publicly available due to laboratory policy.

**Acknowledgments:** The financial support is greatly appreciated.

**Conflicts of Interest:** The authors declare that they have no known competing financial interests or personal relationships that could have appeared to influence the work reported in this paper.

## References

1. Po, C.S. Steel-Plate Encased Concrete Coupling Beams. Ph.D. Thesis, The Hong Kong University of Science and Technology, Hong Kong, China, 2012.
2. Lam, W.Y.; Su, R.; Pam, H.J. Experimental study on embedded steel plate composite coupling beams. *J. Struct. Eng. ASCE* **2005**, *131*, 1294–1302. [CrossRef]
3. Su, R.; Pam, H.J.; Lam, W.Y. Effects of shear connectors on plate-reinforced composite coupling beams of short and medium-length spans. *J. Constr. Steel Res.* **2006**, *62*, 178–188. [CrossRef]
4. Hou, W.; Chen, B.; Guo, Z.X.; Zhang, J. Experimental study on seismic behavior of embedded steel plate reinforced concrete coupling beams. *Civ. Eng. J.* **2017**, *50*, 9–18.
5. Tian, J.B.; Shi, Q.X.; Tao, Y. Research on mechanics and deformation performance of plate-reinforced composite coupling beams with small span-to-depth ratio. *J. Build. Struct.* **2016**, *37*, 83–96.
6. Pi, T.X.; Liu, G.W.; Fu, J.P. Comparative experiment research on seismic behavior of new reinforcement scheme coupling beam with slab. *J. Chongqing Univ.* **2007**, *30*, 107–113.
7. Shin, M.; Gwon, S.W.; Lee, K. Effectiveness of high performance fiber-reinforced cement composites in slender coupling beams. *Constr. Build. Mater.* **2014**, *68*, 476–490. [CrossRef]
8. Canbolat, B.A.; Parra-Montesinos, G.J.; Wight, J.K. Experimental study on seismic behavior of high-performance fiber-reinforced cement composite coupling beams. *ACI Struct. J.* **2005**, *102*, 159–166.
9. Zhao, J.; Li, K.; Shen, F.Q.; Zhang, X.C.; Si, C.Z. An analytical approach to predict shear capacity of steel fiber reinforced concrete coupling beams with small span-depth ratio. *Eng. Struct.* **2018**, *171*, 348–361. [CrossRef]
10. Hu, X.W.; Ding, R.; Zhang, Z.Y.; Fan, J.S. A unified section-based restoring force model for reinforced concrete coupling beams based on the XGBoost model: Establishment, validation and application. *J. Build. Eng.* **2023**, *73*, 106666. [CrossRef]

11. Liang, X.W.; Xing, P.T.; Liu, Z.Z. Experimental study on seismic behavior and shear capacity of FRC coupling beams with small span-to-depth ratio. *J. Build. Struct.* **2016**, *37*, 48–57.
12. Hou, W.; Xu, S.L.; Ji, D.S.; Li, Q.H.; Lin, G. Cyclic performance of steel plate-reinforced high toughness-concrete coupling beams with different span-to-depth ratios. *J. Struct. Eng.* **2018**, *144*, 04018170. [CrossRef]
13. Deng, M.K.; Lu, H.; Song, H.Z. Experimental research on aseismic behavior of high ductile concrete filled steel plate composite coupling beams. *Eng. Mech.* **2019**, *36*, 192–202.
14. Jafari, A.; Shahmansouri, A.A.; Pourshamsian, S.; Bengar, H.A.; Zhou, Y. Post-tensioned coupling beams: Mechanics, cyclic response, and damage evaluation. *Soil Dyn. Earthq. Eng.* **2025**, *188*, 109082. [CrossRef]
15. Szymczak-Graczyk, A.; Ksit, B.; Laks, I. Operational problems in structural nodes of reinforced concrete constructions. *IOP Conf. Ser. Mater. Sci. Eng.* **2019**, *603*, 032096. [CrossRef]
16. Che, J.L.; Han, G.S.; Liang, X.W. Restoring force model of fiber reinforced concrete diagonally reinforced coupling beam with small span-depth ratio. *Earthq. Resist. Eng. Retrofit.* **2017**, *39*, 41–46+40. (In Chinese)
17. Li, Y. Study on Seismic Performance of Ultra-High Toughness Concrete Coupling Beams with Small Span-to-Depth Ratio. Master's Thesis, Southeast University, Nanjing, China, 2019. (In Chinese)
18. Mou, B.; Pan, Y.; Wu, C.L.; Yu, Y.J. Restoring force model for steel beam to CFST/HSS column joints with a reinforced concrete slab. *J. Build. Eng.* **2024**, *82*, 108378. [CrossRef]
19. Song, A.L.; Su, M.Z.; Wang, Z.S.; Wang, L. Experimental study on restoring force model of connection in innovative hybrid coupled wall system. *Build. Struct.* **2015**, *36*, 21–26. (In Chinese)
20. Staszak, N.; Szymczak-Graczyk, A.; Garbowski, T. Elastic analysis of three-layer concrete slab based on numerical homogenization with an analytical shear correction factor. *Appl. Sci.* **2022**, *12*, 9918. [CrossRef]
21. Garbowski, T.; Staszak, N.; Kostrzewski, W.; Szymczak-Graczyk, A. Numerical and experimental validation of homogenization techniques for Bubble Deck slabs. *Civ. Environ. Eng. Rep.* **2025**, *35*, 230–249. [CrossRef]
22. Deng, M.K.; Zhang, M.; Zhang, Y.X. Experimental study on seismic behavior of steel plate high ductile concrete composite coupling beam. *Eng. Mech.* **2020**, *37*, 47–56.
23. Tian, J.B.; Shi, Q.X.; Li, S. Experimental and numerical study of PRC coupling beams with low span-to-depth ratio. *J. Constr. Steel Res.* **2019**, *159*, 34–52. [CrossRef]
24. Tian, J.B.; Zhao, Y.; Tian, P.G. Seismic behavior of plate-reinforced composite coupling beams with RC slabs. *Soil Dyn. Earthq. Eng.* **2023**, *171*, 107984. [CrossRef]
25. Tian, J.B.; Zhao, Y.; Wang, Y.C.; Liu, J.; Du, N.; Jian, Z.; Yuan, Z. Seismic performance and numerical analysis of steel plate-fiber reinforced concrete composite coupling beams. *Structures* **2023**, *48*, 258–274. [CrossRef]
26. *JGJ101-96*; Specification of Testing Methods for Earthquake Resistant Building. China Architecture & Building Press: Beijing, China, 1997. (In Chinese)
27. Lyu, H.; Deng, M.K.; Guo, L.Y. Shear performance of RC beams employing thin-layer ultra-high-ductile concrete permanent formwork (UHDC-PF): Experimental, numerical and theoretical investigations. *Structures* **2026**, *88*, 111926. [CrossRef]
28. Hou, W.; Xu, S.; Ji, D.; Li, Q.; Zhang, P. Seismic performance of steel plate reinforced high toughness concrete coupling beams with different steel plate ratios. *Compos. Part B Eng.* **2019**, *159*, 199–210. [CrossRef]


**Disclaimer/Publisher's Note:** The statements, opinions and data contained in all publications are solely those of the individual author(s) and contributor(s) and not of MDPI and/or the editor(s). MDPI and/or the editor(s) disclaim responsibility for any injury to people or property resulting from any ideas, methods, instructions or products referred to in the content.